



## Article

# Hydrocarbon Accumulation and Overpressure Evolution in Deep–Ultradeep Reservoirs in the Case of the Guole Area of the Tarim Basin

Zhanfeng Qiao <sup>1,2,3</sup> , Tianfu Zhang <sup>1,2,3</sup>, Ruyue Wang <sup>4</sup> , Yahao Huang <sup>5,\*</sup>, Yifan Xue <sup>5</sup>, Jiajun Chen <sup>1,2,3</sup>, Haonan Tian <sup>6</sup>, Anjiang Shen <sup>1,2,3</sup> and Chunsong Si <sup>1,2,3</sup>

<sup>1</sup> PetroChina Hangzhou Research Institute of Geology, Hangzhou 310023, China; qiaozf\_hz@petrochina.com.cn (Z.Q.); zhangtf\_hz@petrochina.com.cn (T.Z.); l1195698829@126.com (J.C.); shenaj\_hz@petrochina.com.cn (A.S.); hyl202405@163.com (C.S.)

<sup>2</sup> CNPC Key Laboratory of Carbonate Reservoir, Hangzhou 310023, China

<sup>3</sup> State Energy Key Laboratory of Carbonate Oil and Gas, Hangzhou 310023, China

<sup>4</sup> Research Institute of Petroleum Exploration and Development, China Petroleum & Chemical Corporation, Beijing 102206, China; wangruiyue.syky@sinopec.com

<sup>5</sup> Hubei Key Laboratory of Petroleum Geochemistry and Environment, Yangtze University, Wuhan 430100, China; xyf257248@163.com

<sup>6</sup> PetroChina Tarim Oilfield Company, Korla 841000, China; 19855681629@163.com

\* Correspondence: hyhtr08916@cug.edu.cn

**Abstract:** Usually, deep oil and gas accumulation is often controlled by strike–slip faults. However, in the Tarim Basin, deep Ordovician oil and gas accumulations are also found in areas far from the fault zone. The process of oil and gas accumulation in deep reservoirs far from strike–slip fault zones is still unclear at present. The source and evolution of Ordovician fluids were analyzed using inclusion geochemical methods and the U–Pb dating technique. The analysis of rare earth elements and carbon–oxygen–strontium isotopes in the reservoirs showed that the reservoirs were weakly modified by diagenetic fluid. The fluid was derived from the fluid formation during the same period as the seawater, and no oxidizing fluid invaded the reservoir. The late oil and gas reservoirs had good sealing properties. The U–Pb dating results combined with homogenization temperature data revealed that the first-stage oil was charged during the Late Caledonian Period, and the second-stage natural gas was charged during the Middle Yanshanian Period. The evolution of the paleo-pressure showed that the charging of natural gas in the Middle Yanshanian was the main reason for the formation of reservoir overpressure. The strike–slip fault zone was basically inactive in the Middle Yanshanian. During this period, the charged natural gas mainly migrated to the reservoir along the unconformity surface and the open strike–slip fault zone in the upper part of the Ordovician reservoir. The source of the fluid shows that the reservoir in the late stage had good sealing properties, and there was no intrusion of exogenous fluid. The overpressure in the reservoir is well preserved at present.

**Keywords:** fluid inclusion; paleo-pressure evolution; paleo-fluid source; deep reservoirs; Tarim Basin



**Citation:** Qiao, Z.; Zhang, T.; Wang, R.; Huang, Y.; Xue, Y.; Chen, J.; Tian, H.; Shen, A.; Si, C. Hydrocarbon Accumulation and Overpressure Evolution in Deep–Ultradeep Reservoirs in the Case of the Guole Area of the Tarim Basin. *Minerals* **2024**, *14*, 790. <https://doi.org/10.3390/min14080790>

Academic Editor: Giovanni Martinelli

Received: 24 May 2024

Revised: 26 July 2024

Accepted: 27 July 2024

Published: 31 July 2024



**Copyright:** © 2024 by the authors. Licensee MDPI, Basel, Switzerland. This article is an open access article distributed under the terms and conditions of the Creative Commons Attribution (CC BY) license (<https://creativecommons.org/licenses/by/4.0/>).

## 1. Introduction

With continuous breakthroughs in oil and gas exploration, the industry has shifted its interest toward deep and ultradeep strata. Currently, the Tarim Basin serves as China’s largest ultradeep oil and gas reservoir, with the Fuman Field being the country’s fastest-producing ultradeep oilfield at the billion-ton level in the deep subsurface domain [1–4]. The strike–slip fault zone’s influence on the reservoir configuration is crucial due to its role in controlling the enrichment, migration, and accumulation of oil and gas [5–8]. The current data show that there is still potential for oil and gas exploration and development inside and outside the strike–slip fault zone. For instance, Well GL2 is not located in a

strike–slip fault zone; however, it achieves a high daily oil production of 25.56 cubic meters per day ( $t^3/d$ ). However, the processes of oil and gas accumulation, the genesis, and the evolution of overpressure away from strike–slip fault zones have not been fully elucidated. This lack of clarity hinders the exploration of deep–ultradeep oil and gas resources in areas far from strike–slip fault zones.

The Fuman oilfield features a vertically developed carbonate reservoir within the strike–slip fault zone characterized primarily by fractures and dissolution cavities. The reservoir hosts a complex history of fluid activity [9–12] intricately linked to the activity of the strike–slip fault zone, which has led to the development of fracture veins within the reservoir. These fractures serve as repositories, preserving invaluable information pertaining to the paleo-temperature, the paleo-pressure, and the oil and gas accumulation processes within the reservoir [13–15]. Furthermore, some studies offer critical insights into the evolution of overpressure and the mechanisms underlying hydrocarbon accumulation in the context of strike–slip fault zones. Fractures can be filled with calcite crystals, and these fracture veins record rich information, such as the temperature–pressure conditions, diagenetic fluid environments, fluid sources, etc. [16–20]. These veins provide windows for low-temperature fluid activity within the sedimentary basin, providing evidence and the characteristics of hydrocarbon fluid migration within source rocks and reservoirs [21–23]. Moreover, they serve as indicators of geological fluid flow patterns and the influence of tectonic movements on fluid dynamics. The fluid inclusions encapsulated within these veins contain a trove of information about the temperature, pressure, fluid type, and composition at the time of mineral growth [24,25]. These inclusions are crucial entry points for revealing insights into paleo-fluid activities and serve as a reliable method for determining fluid activity epochs, paleo-thermal and paleo-pressure conditions, and temporal aspects [26–28]. Importantly, these methods provide an effective means for deciphering the formation epochs of oil and gas reservoirs and the evolutionary processes of overpressure [29–31].

This paper took the Guole area of the Fuman Oilfield as its research object. Based on methods such as characterizing lithofacies, oil inclusion fluorescence spectroscopy, microthermometry, Raman spectroscopy, and the simulation of paleo-inclusion pressures, this study analyzed the evolution of oil and gas overpressure and accumulation in Well GL1 and Well GL2. This research investigated the fluid evolution and hydrocarbon accumulation in reservoirs away from fault zones, focusing on the formation mechanism of Ordovician overpressure and the relationship between overpressure evolution and hydrocarbon accumulation in the Gule area of the Tarim Basin Platform. This study summarizes the hydrocarbon accumulation process and pressure evolution in the non-fault-controlled zone of deep carbonate reservoirs in the Fuman Oilfield, enriches the theory of ancient carbonate hydrocarbon accumulation, and provides important guidance for future exploration decision making and new area expansion.

## 2. Geological Setting

The Fuman Oilfield is located in the Aman Transition Zone in the northern depression of the Tarim Basin (Figure 1). The Aman Transition Zone is bounded to the north by the Tabei Uplift and to the south by the Tazhong Uplift, with its eastern and western boundaries sandwiched between the Manjar Depression and the Awati Depression, respectively. Based on previous analyses of the tectonic evolution of the Tabei Uplift, Tazhong Uplift, and surrounding orogenic belts, the structural evolution of the Aman Transition Zone may have undergone multiple stages [32,33]. During the Early Caledonian (Cambrian), the marginal basins of the Tarim Plate were in an extensional phase, and the overall stress environment within the basin was characterized by extension. The Aman Transition Zone experienced subsidence during this period. In the Middle–Late Caledonian (Mid-Ordovician), the marginal basins ceased expanding and began to subduct beneath the Tarim Plate. The basin experienced a compressional stress regime that persisted into the Early Devonian (Carboniferous), with the Aman Transition Zone undergoing intense and

sustained compression. During the Late Carboniferous–Permian (Late Paleozoic), the closure of the South Tianshan Ocean resulted in the continuous subduction and uplift of the Tarim Northern Uplift, leading to uplift within the Aman Transition Zone as well. During the Indosinian–Yanshanian (Triassic–Cretaceous), the tectonic activity in the basin margins stabilized, and the Aman Transition Zone underwent overall stable subsidence. It reached its definitive configuration during the Himalayan Period (Paleogene–Quaternary). The Ordovician strata in the Aman Transition Zone are well developed and consist of, from bottom to top, the Penglaiba Formation ( $O_{1p}$ ), the Yingshan Formation ( $O_{1-2y}$ ), the Yijianfang Formation ( $O_{2y}$ ), the Tumuxiuke Formation ( $O_{3t}$ ), the Lianglitage Formation ( $O_{3l}$ ), and the Sangtamu Formation ( $O_{3s}$ ). Core-drilling and well-logging data indicate that the primary porosity within the target reservoir is generally not well developed. The main storage spaces are fracture-controlled cavities and vugs influenced by tectonic fracturing and karstification, characterizing a fracture-controlled cavity reservoir [34–36].

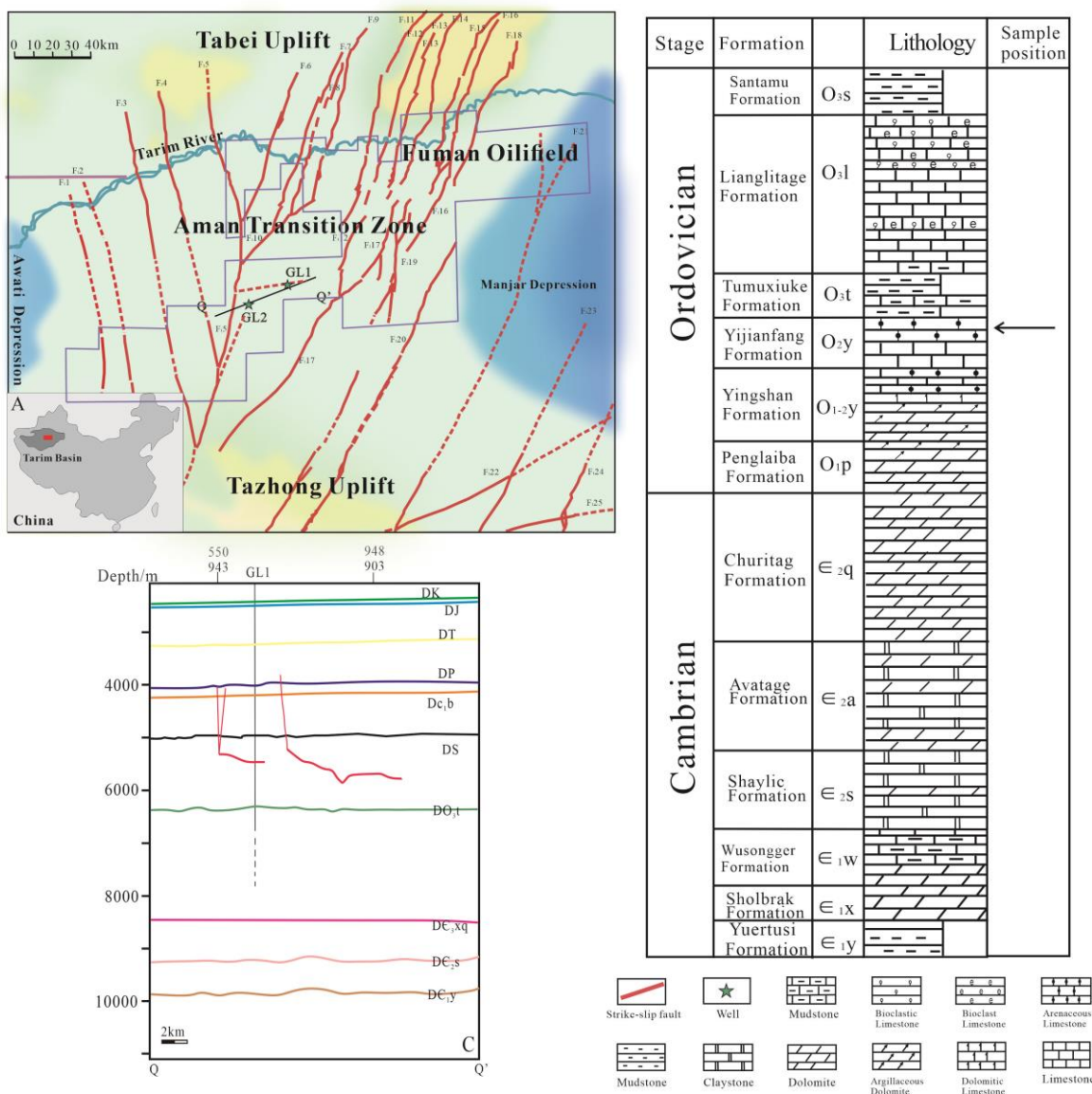


**Figure 1.** Strike-slip fault structure distribution map of the Tarim Basin and Lower Paleozoic stratigraphic histogram of the Guole area.

The main body of the Fuman Oilfield is situated in the subsidence center of the basin’s rift depression system. In the Early Cambrian, the Fuman area inherited the Late Ordovician depression tectonic background and accumulated a series of high-quality

hydrocarbon source rocks from the Yuertusi Formation [37], ranging from continental shelf slopes to basin facies. From the bottom up, the Ordovician system consists of the Penglaiba Formation (O<sub>1p</sub>), Yingshan Formation (O<sub>1-2y</sub>), Yijianfang Formation (O<sub>2y</sub>), Tumuxiuke Formation (O<sub>3t</sub>), Lianglitage Formation (O<sub>3l</sub>), and Santamu Formation (O<sub>3s</sub>). In the Fuman area, the Middle Ordovician Yingshan Formation's first and second members, as well as the Yijianfang Formation, form a continuous sedimentary thickness of approximately 600 m of thick-bedded limestone [38,39]. The O<sub>2y</sub> unit overlays the Late Ordovician massive shale deposits of the mixed shelf, forming a favorable source–reservoir–seal combination and exhibiting significant petroleum resource potential [40,41]. The study area was located in the central part of the Fuman Oilfield. The primary research targets were Well GL1 and Well GL2. Well GL1 was located in the concealed fault zone. Localized structural development was observed, with a formation pressure coefficient of 0.83. Well GL2 was situated north of a secondary northeast-trending fault within the Guole Block, approximately 900 m away from the secondary fault in the northeast direction (Figure 1). It exhibited a formation pressure coefficient of 1.68 and a daily gas production of 28,654 cubic meters.

### 3. Samples and Methods

#### 3.1. Collection of Cores and Data

The samples were primarily collected from the Upper Ordovician Yijianfang Formation carbonate reservoir in Well GL1 and Well GL2 in the Guole area. The core samples corresponded to the upper part of the Yijianfang Formation in the Ordovician system.

#### 3.2. Petrographic Analysis

Micropetrographic observation of fluid inclusions was conducted using an Olympus BX51 microscope and a Nikon-LV100 dual-channel fluorescence-transmission light microscope, and the fluorescence spectrum was obtained with a Maya2000Pro microfluorescence spectrometer. The Linkam (TH-600) heating–cooling stage was used to measure the homogenization temperature ( $T_h$ ) and ice-melting temperature ( $T_m$ ). The control accuracies of the  $T_h$  and  $T_m$  values were  $\pm 1$  °C and  $\pm 0.1$  °C, respectively. Cathodoluminescence (CL) characteristic analysis of the target thin sections was performed using a CL 8200 MK5 cathodoluminescence stage (with an accelerating voltage of 17 kV and beam current of 500  $\mu$ A). Cathodoluminescence images were acquired using a Leica DM2500 microscope under the same exposure time (70 ms) and gain settings (1.005 s).

#### 3.3. Microanalysis of Trace Elements

In situ quantitative elemental analysis was carried out using laser ablation–inductively coupled plasma–mass spectrometry (LA-ICP-MS) with an Agilent at Wuhan Sample Solution Analytical Technology Co., Ltd., Wuhan, China. Helium was employed as the carrier gas, and argon was utilized as the compensation gas to modulate the sensitivity during the laser ablation process. The direct diameter of the laser beam was 100  $\mu$ m, the energy density was 3 J/cm<sup>2</sup>, and the denudation frequency was 10 Hz. Standard samples were calibrated with multiple external standards, and no internal standard was used, employing the glass reference materials BHVO-2G, BCR-2G, and BIR-1G. Each data point of the time-resolved analysis encompassed approximately 20–30 s of the blank signal and 50 s of the sample signal. The ICPMSDataCal10.7 software facilitated the correction of sample signals and the calculation of elemental contents.

#### 3.4. U–Pb Dating of Carbonate Veins

Carbonate rock laser in situ U–Pb isotope dating was conducted at the Radioisotope Laboratory, the University of Queensland, Australia, utilizing an excimer laser ablation system and quadrupole inductively coupled plasma–mass spectrometry (Q-ICP-MS). After the treatment of the post-dolomite pulse sample, the excimer laser was used to etch the dolomite. The laser beam diameter was 200 microns, the frequency was 15 Hz, and the energy density was 1.0 J/cm<sup>2</sup>. The laser ablation material used helium as the carrier

gas, while argon and nitrogen were auxiliary gases that enhanced the signal strength. A sample point encompassed 20 s of background acquisition, 25 s of data acquisition, and 10 s of sample cleaning. The standard sample NIST 612 reference glass and stable  $^{43}\text{Ca}$  isotope served as the internal standard for the trace element calibration in calcite. NIST614 was primarily used for instrument sensitivity and  $^{207}\text{Pb}/^{206}\text{Pb}$  ratio correction. AHX-1, a standard sample with an age of 209.8 Ma, mainly contains corrected  $^{238}\text{U}/^{206}\text{Pb}$  ratios. The data were processed with the LoliteV3.4 software developed by the University of Melbourne, Australia, and the generation of calcite U–Pb age harmonics maps was performed with the IsoplotV3.76 software developed by the Berkeley Center for Geochronology.

### 3.5. Paleo-Pressure Calculation of Gas- and Oil-Bearing Inclusions

The  $\text{CH}_4$  gaseous and dissolved aqueous fluid inclusions were all quantified by Raman spectroscopy using a JY/Horiba LABRAM HR800 instrument equipped with  $20\times$ ,  $50\times$ , and  $100\times$  long-focus objectives and a 532 nm green laser with a 200–500 mW output power at the China University of Geosciences (Wuhan). The spectral collection was performed with a split width of  $100\ \mu\text{m}$  and a  $300\ \text{gr}\cdot\text{mm}^{-1}$  optical grating with a  $2650\ \text{cm}^{-1}$  grating center. A total of 200–500 accumulations were used for each spectrum to ensure the highest signal-to-noise ratio needed to calculate the peak area ratio of water– $\text{CH}_4$ . All the spectra needed to be corrected by the baseline in advance to ensure that the initial peak intensity was zero. An  $1800\ \text{gr}\cdot\text{mm}^{-1}$  grating/ $50\ \mu\text{m}$  split width was adopted to acquire accurate Raman shifts for individual gaseous inclusions. Neon lamp signals were simultaneously collected to determine the Raman wavenumbers.

These high-resolution techniques were used to capture precise wavenumber shifts and peak area ratios (PARs) so that the density of pure  $\text{CH}_4$  inclusions and the  $\text{CH}_4$  concentration could be calculated by measuring the C–H symmetric stretching band ( $\nu_1$ ) of  $\text{CH}_4$  in homogenized states. The peak areas were integrated by Gauss–Lorentz interactions. The density and  $T_h$  of the fluid inclusions in different systems of thermodynamic models were used to calculate the trapping pressure of the fluid inclusions.

Individual oil inclusion gas–liquid ratios were acquired through oil inclusion co-focusing microscopy section scanning. By utilizing the isochore intersection method with the homogenization temperatures of the oil inclusions and coexisting aqueous salt inclusions, the minimum trapping pressure of the oil inclusions was calculated.

### 3.6. Basin Model

Integrated with the logging lithology and stratigraphic data, the burial–thermal history could be simulated by the BasinMod-1D software. The measured values of the vitrinite reflectance and temperature in the borehole were all provided by the PetroChina Tarim Oilfield Company to calibrate the modeling results.

## 4. Results and Discussion

### 4.1. Developmental Stages of Veins

Using cathodoluminescence (CL) and transmitted-light observation, the developmental stages of the veins in the Ordovician Yijianfang Formation carbonate reservoir in the study area were determined [42]. Calcite, bitumen, and siliceous materials were found to be more common fillings. The samples collected from Well GL2 in the Guole area predominantly exhibited calcite as the primary mineral component within the veins. No distinct multistage vein crosscutting relationships were observed with the development of two types of veins: vug-filling calcite veins and extensional veins (Figure 2a,b). Similarly, the samples from Well GL1 in the Guole area primarily displayed calcite as the mineral composition within the vein bodies. Although vein-crosscutting relationships were absent, the main development involved the dissolution of pore-type filled veins (Figure 2c). The analysis of the collected samples showed that the color of the cathodic luminescence of the veins filling the two wells was similar, mainly dark red (Figure 2g,i,k). No clear evidence of multistage development was observed (Figure 2d–k), indicating the presence of only

one-stage calcite vein bodies. The calcite veins were widely developed in the study area. The edges of the veins were not straight, and the width of the veins was 0.2–0.5 cm. At this stage, veins were always in contact with surrounding rocks, the sizes of crystals were different, and there was no obvious recrystallization. Silicification phenomena were observed in samples from Well GL2.

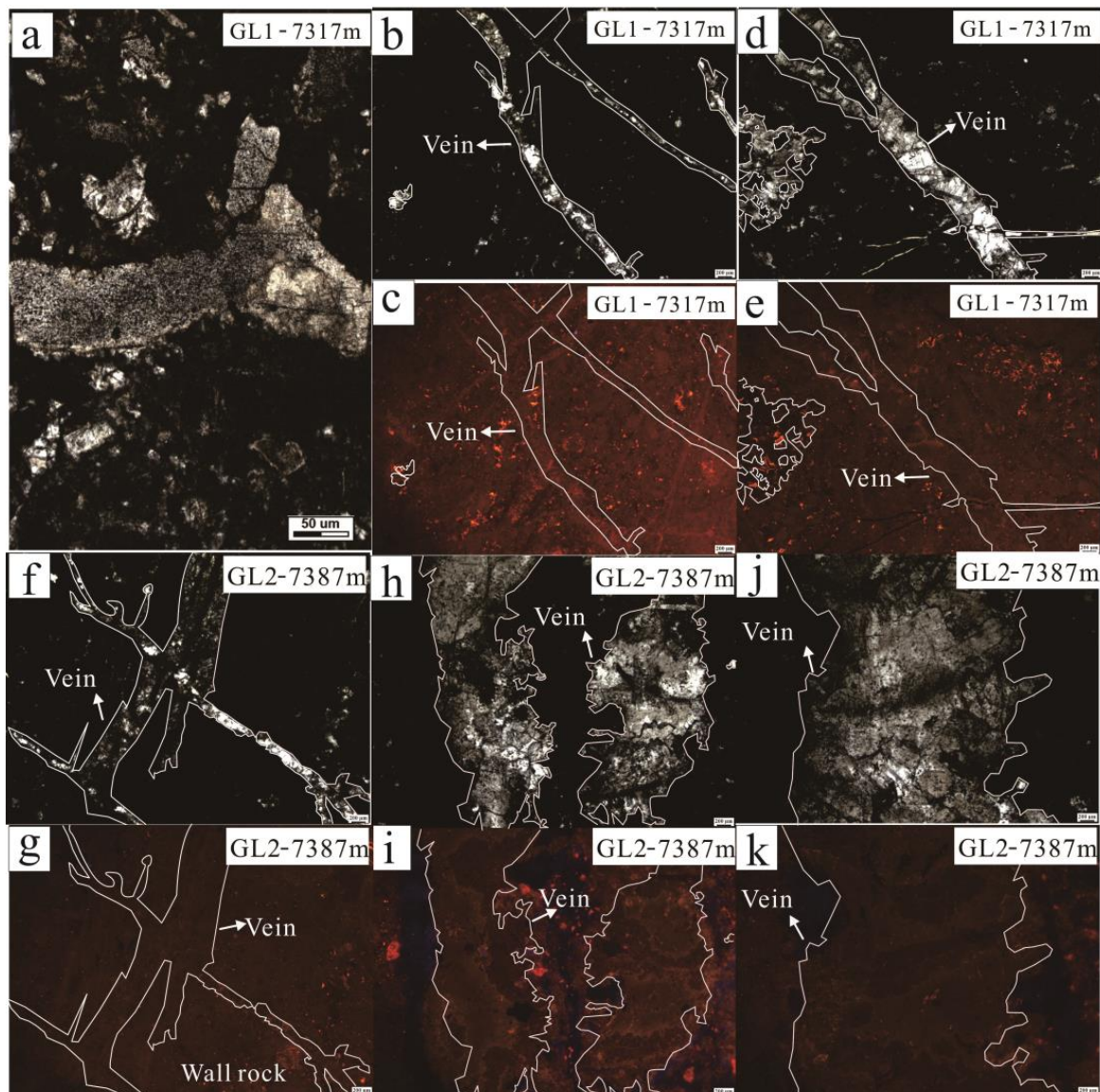


**Figure 2.** Transmitted-light and cathodoluminescence images of calcite veins in carbonate rock samples from the Guole area. (a,b,d): Transmission light photographs of calcite vein body in well GL1. (c,e): Cathode luminescence photographs of calcite vein body in well GL1. (f,h,j): Transmission light photographs of calcite vein body in well GL2. (g,i,k): Cathode luminescence photographs of calcite vein body in well GL2.

#### 4.2. Fluid Source of Fracture-Filling Veins

Rare earth elements can enter the crystal lattice of carbonate minerals by substituting  $\text{Ca}^{2+}$ ; thus, they are capable of reflecting the source of the rock-forming fluids [43–45]. Different fluid sources exhibit distinct rare earth element partitioning patterns, which can be used to infer the nature and origin of the fluids based on the shapes of the partitioning patterns. In situ elemental analysis of the micro-areas in the calcite vein samples from Wells GL1 and GL2 was conducted after standardization with chondrites for trace element analy-

sis. The results are shown in Figure 3. Wells GL1 and GL2 exhibited light rare earth element (LREE) enrichment and heavy rare earth element (HREE) deficiency, indicating a typical diagenesis linked to the seawater environment. In the Well GL1 samples, the  $\Sigma$ REE ranged from 19.8784 to 37.4335; the  $\delta$ Ce values varied from 0.65175 to 0.93785, with an average of 0.73725, indicating a slightly negative anomaly; the  $\delta$ Eu values varied from 0.650585 to 0.89437, with an average of 0.708538; and the Y/Ho values ranged from 34.60 to 41.35, with an average of 36.33. In the Well GL2 samples, the  $\Sigma$ REE contents ranged from 3.2178 to 4.9122; the  $\delta$ Ce values varied from 0.685521 to 0.726968, with an average of 0.705049, indicating a slightly negative anomaly; the  $\delta$ Eu values varied from 0.53267 to 0.805952, with an average of 0.651971; and the Y/Ho values ranged from 33.82 to 42.63, with an average of 38.08.

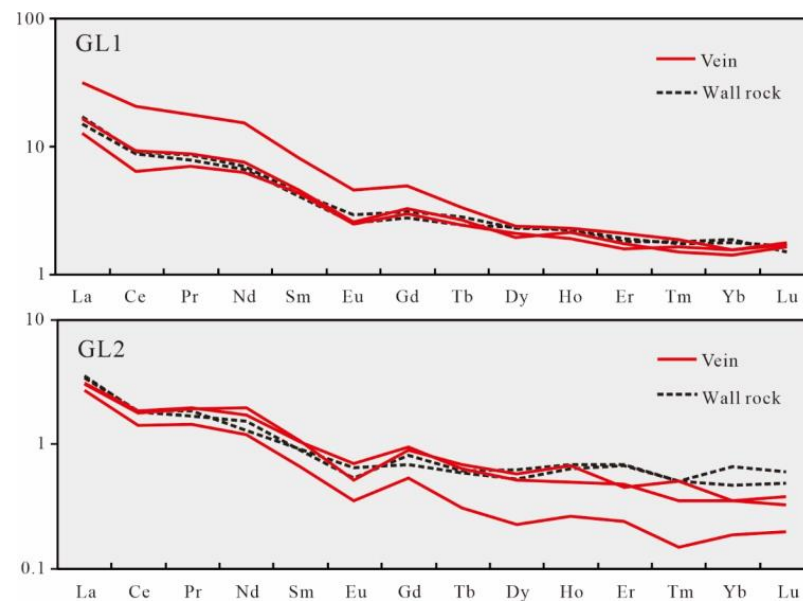


**Figure 3.** Rare earth element partitioning model of calcite samples from Wells GL1 and GL2 in Guole area.

#### 4.3. Fluid Inclusion Characteristics

The transmission light and fluorescence microscopic observations showed that the developed oil and gas inclusions were trapped in the calcite vein in the Guole area, which were all developed in the calcite veins of the first stage. Two different types of oil inclusions could be distinguished by fluorescence observation: in Well GL1, pale-blue fluorescent oil inclusions were evident (Figure 4a), while in Well GL2, blue–green fluorescent oil inclusions were observed (Figure 4b). The blue–green oil inclusions were primarily located within calcite grains, displaying an isolated distribution and representing primary oil inclusions. These inclusions were relatively large in size, ranging mainly from 5 to 10  $\mu$ m, with elongated and elliptical shapes being dominant. The pale-blue fluorescent oil inclusions were mainly found within calcite fractures and exhibited linear distributions and secondary oil inclusions. These inclusions were relatively small in size, ranging primarily from 3 to 6  $\mu$ m, with elongated and irregular shapes being dominant. Secondary gaseous inclusions could be seen under transmitted light (Figure 4c,d). The fluorescence spectra of the oil inclusions with different colors were recorded, and the  $\lambda_{\max}$  and  $QF535$  values were calculated (Figure 5) [46–49]. The  $\lambda_{\max}$  values of most blue–green fluorescent oil inclusions were in the range of 511–540 nm; the corresponding  $QF535$  values were in the range of 1.12–1.49; and the API of the oil inclusions was in the range of 30.5–33.0, indicating a greater proportion of large molecular components within the inclusions and the lower maturity of the enclosed oil. The  $\lambda_{\max}$  values of most pale-blue fluorescent oil inclusions are in the range of 482–495 nm, corresponding  $QF535$  values are in the range of 0.62–0.91, and the API of the oil inclusions was in the range of 35.0–38.6, indicating a greater proportion of

small molecular components within the inclusions and greater maturity of the enclosed oil. Combining these observations with the reservoir facies analysis of the fluid inclusions, it can be inferred that the early-charged oil in the Ordovician reservoir primarily exhibited blue–green fluorescence, representing relatively immature oil, while the late-charged oil exhibited pale-colored fluorescence, representing relatively mature oil.

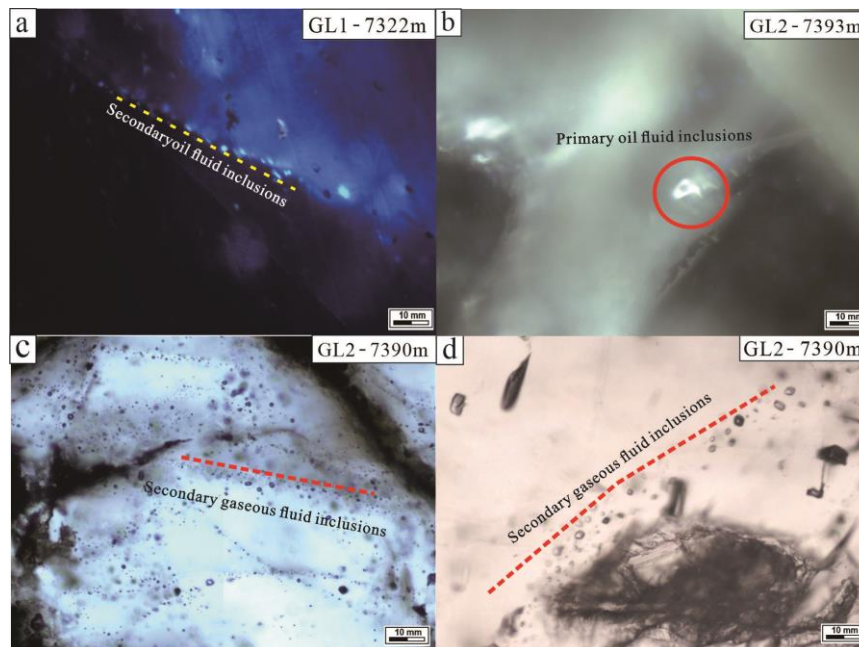


**Figure 4.** (a) Fluorescence photograph of light-blue fluorescent crude oil inclusion in Well GL1; (b) fluorescence photograph of blue–green fluorescent crude oil inclusion in Well GL2; (c,d) transmitted-light photographs of secondary gas inclusion in Well GL2.

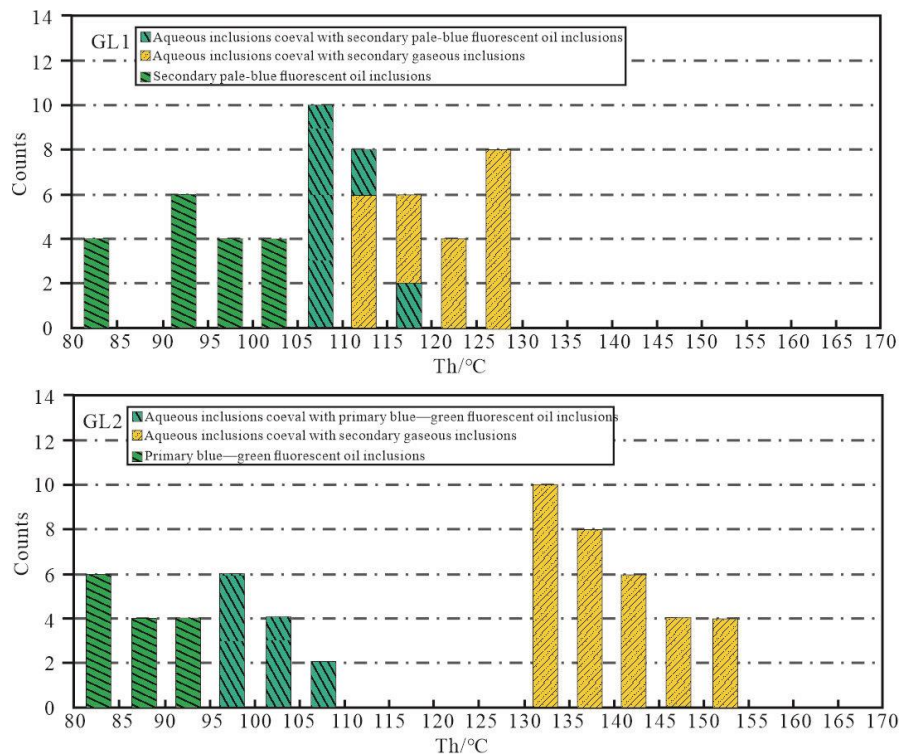


**Figure 5.** Distribution of homogenization temperatures for oil inclusions coexisting with aqueous inclusions in calcite veins of Ordovician reservoirs in the Guole area.



Microthermometry was conducted on coexisting fluid inclusions of oil and gas within the developed calcite veins of the samples from the two wells in the Guole area, as shown in Figure 5. The homogenization temperature distribution of the secondary pale-blue fluorescent oil inclusions in the calcite vein of the Ordovician reservoir in Well GL1 ranged from 81.2 °C to 103.4 °C; that of the aqueous inclusions coeval with the secondary pale-blue fluorescent oil inclusions ranged from 107.1 °C to 118.9 °C; and that of the aqueous inclusions coeval with the secondary gaseous inclusions ranged from 110.6 °C to 128.8 °C. The homogenization temperature distribution of the primary blue–green fluorescent oil inclusions in the Ordovician calcite vein of Well GL2 ranged from 83.1 to 93.5 °C; that of the aqueous inclusions coeval with the primary blue–green fluorescent oil inclusions ranged from 97.2 °C to 107.3 °C; and that of the aqueous inclusions coeval with the secondary gaseous inclusions ranged from 133.5 °C to 152.5 °C. The salinity of the aqueous inclusions coeval with the blue–green fluorescent primary oil inclusions in Well GL2 varied between 10.1% and 24.1%, with an average of 15.0%. The salinity of the aqueous inclusions coeval with the pale-blue fluorescent primary oil inclusions in Well GL1 varied between 8.2% and 13.6%, with an average of 11.4%.

#### 4.4. Oil and Gas Accumulation Time

On the basis of systematic micropetrography, microthermometric analysis of the fluid inclusions in the diagenetic minerals of reservoirs, carbonate U–Pb dating, the period of hydrocarbon fluid charging, and the accumulation time can be determined by combining the reservoir burial history and thermal evolution history with the  $T_h$  of the saline inclusions coexisting with the hydrocarbon inclusions and the hydrocarbon generation history of the main source rock. During the burial process, especially when the paleogeothermal temperature exceeds the trapping temperature of the inclusions, the inclusions rupture due to excessive internal pressure, undergo thermal re-equilibrium—such as stretching, fluid leakage, or fluid refilling—and, finally, heal again, resulting in an increase in the homogenization temperature of the inclusions. Many factors, such as the size of the inclusion, the shape of the inclusion, and the composition of the inclusion, affect the degree of rebalancing. In addition, there are several subjective interference factors in the selection of inclusions and the determination of the homogenization temperature. Therefore, when fluid inclusions are used to determine the hydrocarbon accumulation time of Ordovician reservoirs in the Guole area, it may be more reliable to select the minimum homogenization temperature of aqueous inclusions coeval with oil inclusions and determine the hydrocarbon accumulation time in combination with the reservoir burial history and thermal evolution history. The minimum  $T_h$  values are the real  $T_h$  values, whereas the higher  $T_h$  values are the ones modified during re-equilibration. The homogenization temperature data from the carbonate reservoir samples of the Yijianfang Formation in the Ordovician reservoir in the Guole area in Figure 6 were projected onto the burial history. The minimum homogenization temperatures of the aqueous inclusions coeval with the light-blue fluorescent crude oil inclusions were plotted onto the burial history. The entrapment time of the obtained inclusions was approximately 390–400 Ma. The dating results show that the vein in Well GL2 formed at  $395 \pm 21$  Ma (Figure 7). The minimum homogenization temperatures of the saline inclusions coeval with the secondary gas inclusion were plotted onto the burial history, and the trapping time of the inclusions was approximately 160–140 Ma (Figure 7).

#### 4.5. Paleo-Pressure Recovery

Thirteen individual oil inclusions with diameters of greater than 5  $\mu\text{m}$ , representing both gas and liquid phases and capable of generating oil inclusion bubble-filling degree measurements, were selected for minimum trapping pressure reconstruction in conjunction with coexisting aqueous inclusions (Figure 8). Three-dimensional models were reconstructed for oil inclusions of different fluorescence colors to obtain the volume parameters of the individual oil inclusions. The compositions of the individual oil inclusions were

deduced based on the functional relationship between the homogenization temperature ( $T_{Hoil}$ ) and the degree of bubble filling ( $F_v$ ) at room temperature.

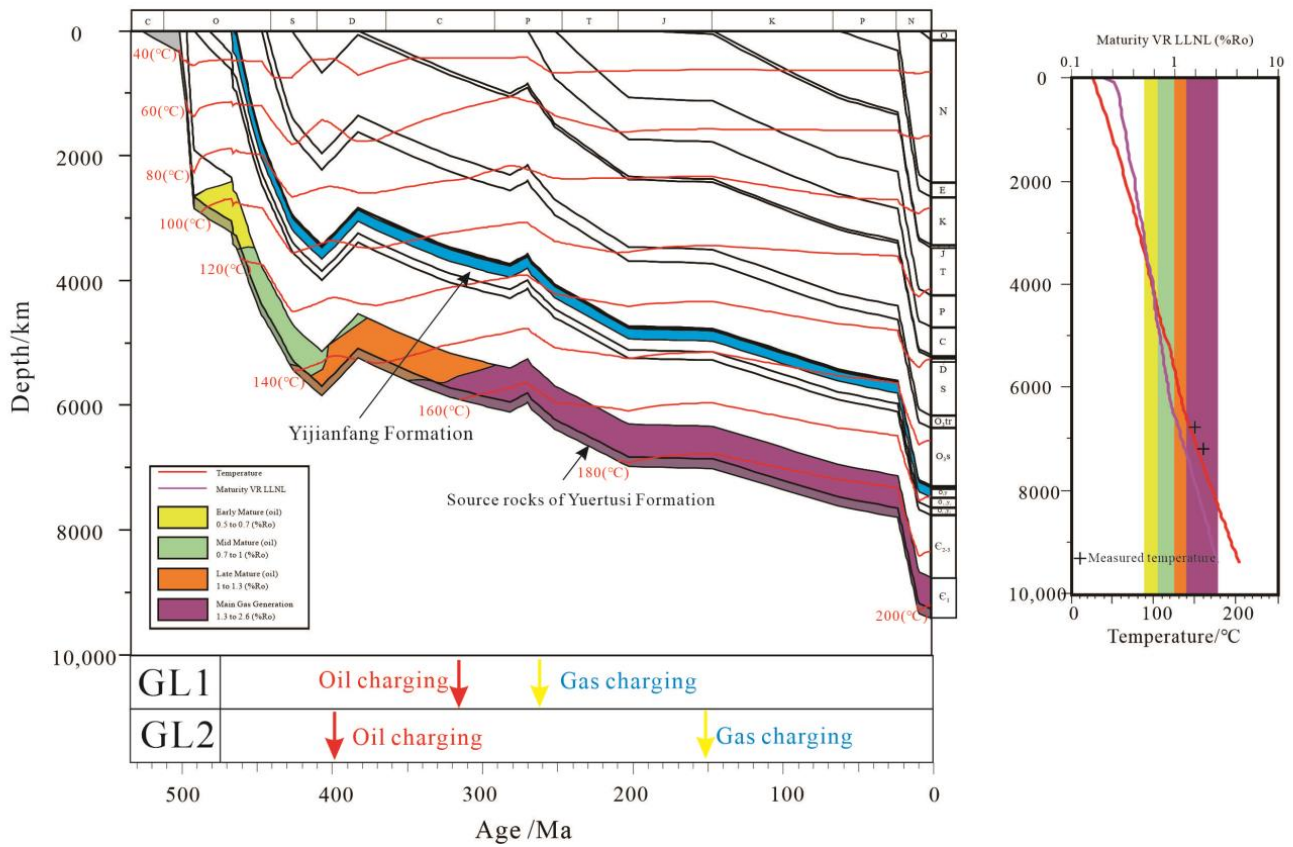


Figure 6. Burial-thermal-hydrocarbon generation history of the strike-slip fault zone in the Guole area.

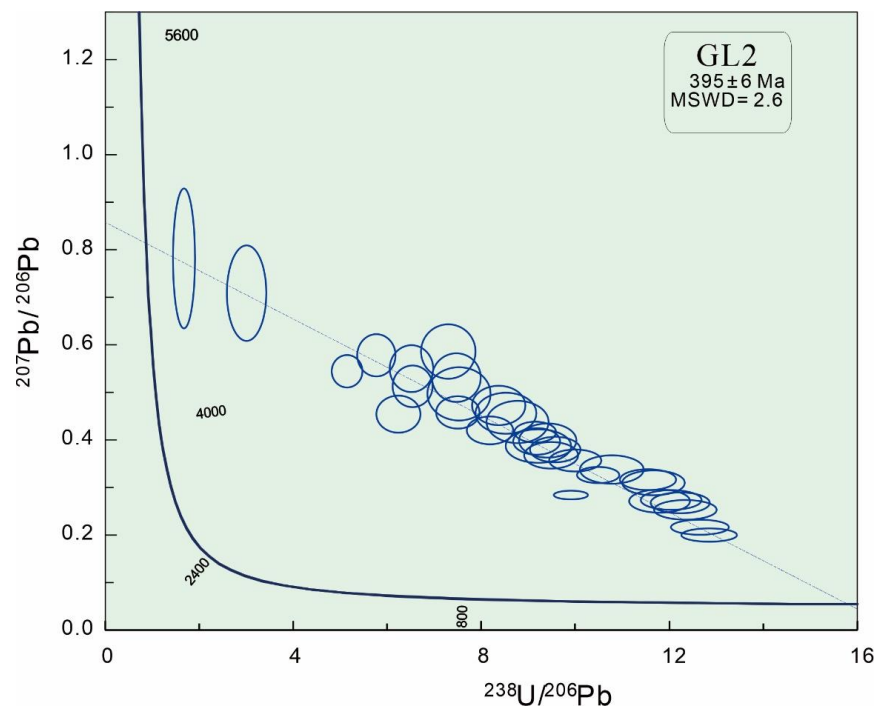
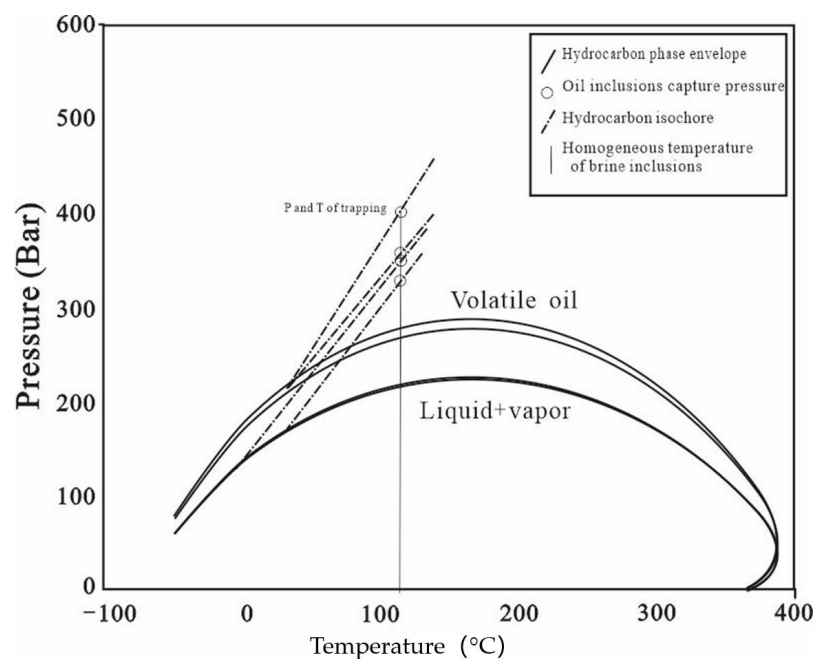


Figure 7. U-Pb isotope dating of isochrons in calcite veins with primary oil inclusions from Well GL2.



**Figure 8.** Simulation curves of the minimum trapping pressure of oil inclusions in the calcite veins of the Ordovician Yijianfang Formation in the Guole area.

Using the obtained parameters, including the homogenization temperatures of both the oil and coexisting aqueous inclusions, the composition of the oil inclusions, and the bubble-filling degrees, the minimum trapping pressure of the inclusions was simulated using the PVTsim software. The simulation results show that the homogenization temperature of the pale-blue oil inclusions in Well GL1 ranged from 84.1 to 102.1 °C, the trap pressure ranged from 28.7 to 35.0 MPa, and the pressure coefficient ranged from 0.90 to 1.09 (Table 1). The homogenization temperature of the blue-green oil inclusion in Well GL2 ranged from 81.4 to 87.1 °C, the trapping pressure ranged from 31.7 to 40.0 MPa, and the pressure coefficient ranged from 0.91 to 1.18 (Table 1).

**Table 1.** Paleo-pressure statistics of oil inclusions in Ordovician reservoirs in the Guole area of the Fuman Oilfield. °C temperature.

Well	Depth (m)	$T_{oil}$ (°C)	Gas-Liquid Ratio	$T_{haq}$ (°C)	Trapping Pressure (MPa)	Pressure Coefficient
GL1	7325	84.1	11	108.7	35.0	1.09
GL1	7317	87.2	12	102.5	31.1	0.94
GL1	7317	91.4	9	113.4	30.6	0.93
GL1	7317	92.1	12	104.6	29.4	0.92
GL1	7317	93.5	11	114.2	32.1	1.00
GL1	7325	102.1	11	117.6	28.7	0.90
GL2	7390	81.4	13	96.8	32.6	0.93
GL2	7390	84.2	9	106.4	31.7	0.91
GL2	7390	83.2	10	108.7	34.5	1.01
GL2	7393	87.1	12	121	40.0	1.18

Laser Raman spectroscopy enables the investigation of the gas-, liquid-, and solid-phase components of fluid inclusions in calcite and quartz veins and allows for the paleo-pressure reconstruction of gas inclusions. The methane stretching vibration peak shift range of the methane gas inclusions in the calcite from Well GL1 was 2912.53–2912.76  $cm^{-1}$ , while in the calcite from Well GL2, it ranged from 2911.01 to 2911.12  $cm^{-1}$ . By utilizing the methane peak shifts obtained via laser Raman spectroscopy (Table 2), the densities of the corresponding gas inclusions could be calculated. Figure 9 shows the Raman spectra of the typical methane gas inclusions in calcite veins from the Yijianfang Formation in the Guole area. Based on the distribution range of the Fermi doublet spacing obtained from

the laser Raman measurements of the CH<sub>4</sub> inclusions, the corresponding densities of the CH<sub>4</sub> inclusions were calculated. For the calcite veins from Well GL1, the density of the CH<sub>4</sub> inclusions ranged from 0.1880 to 0.2650 g/cm<sup>3</sup>, while for the calcite veins from Well GL2, the density range was 0.2640 to 0.2694 g/cm<sup>3</sup> (Table 2). Using the obtained density and homogenization temperature information, a thermodynamic model was employed to calculate the trapping pressure of the CH<sub>4</sub> inclusions (Table 2). The maximum trapping pressure of the CH<sub>4</sub> inclusions in the calcite from Well GL1 was 44.73 MPa, with a minimum value of 42.06 MPa, corresponding to a pressure coefficient of 1.05–1.12. In the calcite from Well GL2, the maximum trapping pressure of the CH<sub>4</sub> inclusions was 87.50 MPa, with a minimum value of 83.75 MPa, corresponding to a pressure coefficient of 1.68–1.75.

**Table 2.** Paleo-pressure statistics of Ordovician gas inclusions in the Guole area of the Fuman Oilfield.

Well	Depth (m)	$\nu_{\text{true}}$ (cm <sup>-1</sup> )	Density (g/cm <sup>3</sup> )	$T_h$ (°C)	Trapping Pressure (MPa)	Pressure Coefficient
GL1	7317	2912.53	0.2650	111.3	44.65	1.12
GL1	7317	2912.58	0.1960	111.3	43.87	1.10
GL1	7317	2912.53	0.1982	111.3	44.65	1.12
GL1	7317	2912.65	0.1929	115.2	42.81	1.07
GL1	7317	2912.61	0.1947	115.2	43.56	1.09
GL1	7317	2912.75	0.1885	115.2	42.06	1.05
GL1	7317	2912.76	0.1880	116.4	42.14	1.05
GL1	7317	2912.59	0.1955	116.4	44.73	1.12
GL2	7390	2911.03	0.2684	133.5	86.79	1.74
GL2	7390	2911.02	0.2689	133.5	87.14	1.74
GL2	7390	2911.01	0.2694	133.5	87.5	1.75
GL2	7390	2911.03	0.2684	133.5	86.79	1.74
GL2	7390	2911.05	0.2674	133.8	86.18	1.72
GL2	7390	2911.05	0.2674	133.8	86.18	1.72
GL2	7390	2911.12	0.2640	133.8	83.75	1.68
GL2	7390	2911.05	0.2674	133.8	86.18	1.72
GL2	7390	2911.06	0.2670	133.8	85.83	1.72
GL2	7390	2911.09	0.2655	135.6	85.4	1.71
GL2	7390	2911.1	0.2650	135.6	85.06	1.70
GL2	7390	2911.08	0.2660	135.6	85.75	1.72
GL2	7390	2911.08	0.2660	135.6	85.75	1.72
GL2	7390	2911.07	0.2665	135.6	86.1	1.72

$T_h$ : Homogenization temperatures of aqueous inclusions coeval with pure CH<sub>4</sub> inclusions.

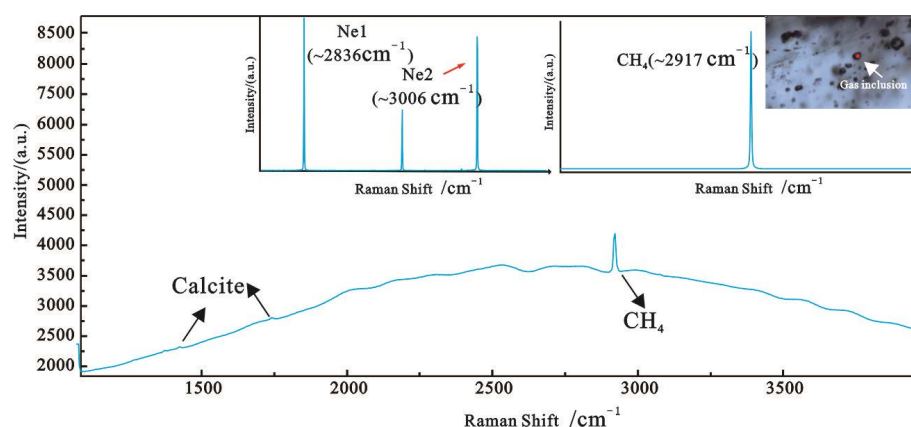


**Figure 9.** Raman spectra of CH<sub>4</sub> inclusions in calcite veins of the Ordovician Yijianfang Formation in the Guole area.

Through the paleo-pressure simulation of the fluid inclusions and Raman spectroscopy, the paleo-pressure evolution of the Ordovician reservoir in Well GL1 was determined as follows (Figure 10): During the Early Hercynian Period (approximately 320 Ma), a first-stage entrapping of light-blue oil inclusions occurred under normal pressure conditions, with a pressure coefficient ranging from 0.9 to 1.09. Second-stage natural gas charging took place during the Late Hercynian Period (approximately 260 Ma), during which the

reservoir pressure remained at normal levels, with a pressure coefficient ranging from 1.05 to 1.12. For the Ordovician reservoir in Well GL2, the paleo-pressure evolution was characterized by the following phases: During the Early Hercynian Period (approximately 402 Ma), the first stage of entrapment of blue–green oil inclusions occurred under normal pressure conditions, with a pressure coefficient ranging from 0.91 to 1.18 (Table 1). The second-stage natural gas charging occurred during the Yanshanian Period (approximately 150 Ma), resulting in overpressure conditions in the reservoir. In the Indosinian–Yanshanian Period, Well GL2 experienced the charging of oil-cracking gases derived from Lower Cambrian salt, leading to the development of high overpressure. During the Yanshanian Period, the pressure coefficient exceeded 1.60, reaching a maximum of 1.75, and this overpressure state persisted until the present (Figure 10). Yanshanian gas charging was identified as the primary cause of overpressure formation in Well GL2. Due to the complexity of fault development, the sequence of oil and gas maturation, and the different migration paths, there were different oil and gas characteristics in adjacent wells in the same area, resulting in the main condensate in Well GL1 and gas in Well GL2. Well GL1 remains at normal pressure, and Well GL2 is currently under pressure in different production environments.

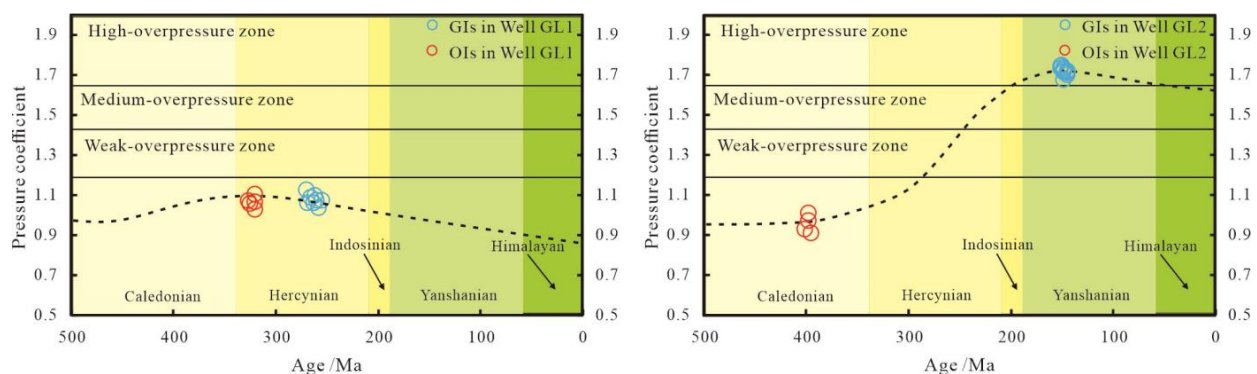


**Figure 10.** Pressure evolution restoration map of the Ordovician Yijianfang Formation in the Guole area.

#### 4.6. Fault Activity and Hydrocarbon Accumulation

The fault activity in the Guole area of the Fuman oilfield in the Tarim Basin has undergone several geological periods, including the Middle Caledonian (475–450 Ma), Middle–Late Caledonian (450–430 Ma), Late Caledonian (430–390 Ma), and Middle–Late Hercynian (320–260 Ma). The strike–slip fault zone was first formed in the Middle Ordovician and was initially characterized as an upright linear fault with a relatively small scale (Figure 11), and fractured vuggy reservoirs were widely developed. At this time, the source rock of the Yuertusi Formation had just reached the hydrocarbon generation stage and began to release hydrocarbons. The first phase of low-maturity crude oil (API:30.5–33.0) migrated upward to the Middle–Upper Ordovician along the vertical fracture, and a large amount of low-maturity crude oil was charged into the reservoir. In the Early Hercynian Period (390–350 Ma), tectonic uplift and the reactivity of the strike–slip fault in the northwest led to the formation of new fractures and caverns, and the calcite filled with fractures and caverns broke under the action of this tectonic activity. At the end of the Devonian Period, the tectonic uplift basically ended, and the source rocks of the Yuertusi Formation, as a whole, reached the stage of high-maturity hydrocarbon generation. High-maturity oil and gas (API:30.5–33.0) migrated to the Ordovician reservoirs along active strike–slip faults to accumulate (Figure 12). The reactivity in the Early Indosinian–Yanshanian fault zone provided key transport channels for deep geological fluids and oil and gas charging. Hydrothermal fluids or organic acid fluids with corrosion effects transformed the reservoir space along the fault zone, fractures, or connected pores, forming new oil and gas accumulation sites. A large amount of dry gas was injected into the reservoir on a large scale. Crude oil accumulation occurred mainly in the Late Caledonian, which was the period with the highest rate of strike–slip fault tectonic activity.

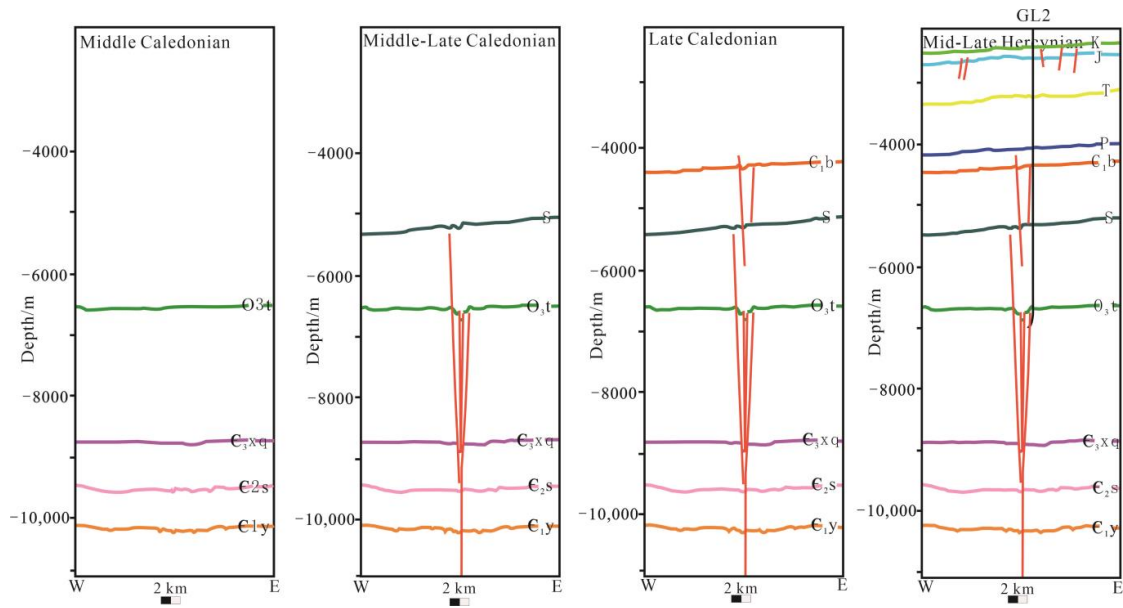
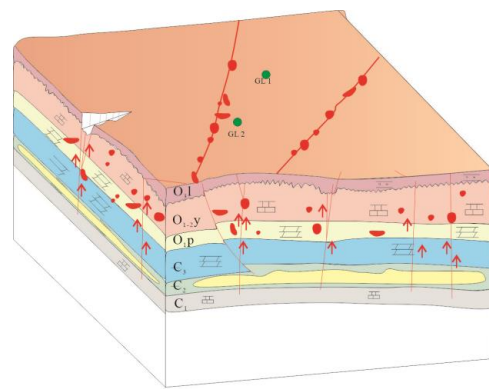
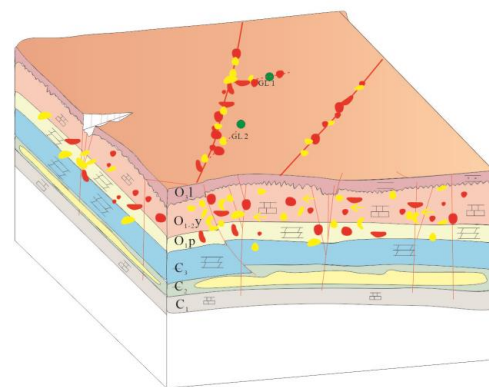


Figure 11. Strike-slip fault activity period and growth process diagram.



a. MIDDLE—LATE Caledonian



b. EARLY—MIDDLE Yanshanian

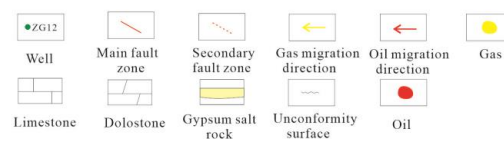


Figure 12. Oil and gas accumulation model in Guole area. (a) Middle and Late Caledonian hydrocarbon accumulation model in Guole area. (b) Early and Middle Yanshanian hydrocarbon accumulation model in Guole area.

The evolution of the late stage had good sealing properties, and there was no intrusion of exogenous fluid. The overpressure in the reservoir is well preserved at present.

## 5. Conclusions

1. The analysis of cathodoluminescence and rare earth elements in the Guole area showed that the reservoir only developed first-stage calcite veins, the color of the cathodoluminescence was dark red, the total amount of rare earth elements was low, the light rare earth elements (LREEs) were rich, and the heavy rare earth elements (HREEs) were lacking, which belonged to a typical marine diagenetic environment. No oxidized fluid intruded into the reservoir.
2. The U–Pb dating results revealed that calcite veins containing primary oil-bearing inclusions formed at  $395 \pm 21$  Ma. The comprehensive temperature data revealed that the first-stage oil was charged during the Late Caledonian Period, and the second-stage natural gas was charged during the Middle Yanshanian Period.
3. The evolution of the paleo-pressure showed that the charging of natural gas in the Middle Yanshanian was the main reason for the formation of reservoir overpressure. The strike–slip fault zone was basically inactive in the Middle Yanshanian. During this period, the charged natural gas mainly migrated to the reservoir along the unconformity surface and the unenclosed strike–slip fault zone in the upper part of the Ordovician reservoir. The source of the fluid showed that the reservoir in the late stage had good sealing properties, and there was no intrusion of exogenous fluid. The overpressure in the reservoir is well preserved at present.

**Author Contributions:** Data curation, T.Z., R.W. and Y.X.; Methodology and Visualization, J.C., H.T., A.S. and C.S.; Review and Editing, Z.Q. and Y.H.; Funding acquisition, Y.H. and Z.Q. All authors have read and agreed to the published version of the manuscript.

**Funding:** This work was funded by the National Natural Science Foundations of China (no. 42372169; no. 42302154).

**Data Availability Statement:** Detailed information describing the experimental data is in the main text.

**Acknowledgments:** We acknowledge the precious advice of the editors and reviewers.

**Conflicts of Interest:** The paper reflects the views of the scientists and not the company which the co-author Haonan Tian is employed by.

## References

1. Kihle, J. Adaptation of fluorescence excitation-emission microspectroscopy for characterization of single hydrocarbon fluid inclusions. *Org. Geochem.* **1995**, *23*, 1029–1042. [[CrossRef](#)]
2. Song, X.; Chen, S.; Xie, Z.; Kang, P.; Li, T.; Yang, M.; Liang, M.; Peng, Z.; Shi, X. Strike-slip faults and hydrocarbon accumulation in the eastern part of Fuman oilfield, Tarim Basin. *Oil Gas Geol.* **2023**, *44*, 335–349.
3. Wang, Y.; Chang, X.; Sun, Y.; Shi, B.; Qin, S. Investigation of fluid inclusion and oil geochemistry to delineate the charging history of Upper Triassic Chang 6, Chang 8, and Chang 9 tight oil reservoirs, Southeastern Ordos Basin, China. *Mar. Petrol. Geol.* **2020**, *113*, 104115. [[CrossRef](#)]
4. Wang, P.; Wang, G.; Chen, Y.; Hao, F.; Yang, X.; Hu, F.; Zhou, L.; Yi, Y.; Yang, G.; Wang, X.; et al. Formation and preservation of ultradeep high-quality dolomite reservoirs under the coupling of sedimentation and diagenesis in the central Tarim Basin, NW China. *Mar. Petrol. Geol.* **2023**, *149*, 106084. [[CrossRef](#)]
5. Han, X.; Deng, S.; Tang, L.; Cao, Z. Geometry, kinematics and displacement characteristics of strike-slip faults in the northern slope of Tazhong uplift in Tarim Basin: A study based on 3D seismic data. *Mar. Petrol. Geol.* **2017**, *88*, 410–427. [[CrossRef](#)]
6. Ma, A.; Jin, Z.; Zhu, C.; Bai, Z. Cracking and thermal maturity of Ordovician oils from Tahe Oilfield, Tarim Basin, NW China. *J. Nat. Gas. Geosci.* **2017**, *2*, 239–252. [[CrossRef](#)]
7. Yang, X.; Tian, J.; Wang, Q.; Li, Y.L.; Yang, H.; Li, Y.; Tang, Y.; Yuan, W.; Huang, S. Geological understanding and favorable exploration fields of ultradeep formations in Tarim Basin. *China Pet. Explor.* **2021**, *26*, 17–28.
8. Zhang, S.; Jin, Q.; Sun, J.; Wei, H.; Cheng, F.; Zhang, X. Formation of hoodoo-upland on Ordovician karst slope and its significance in petroleum geology in Tahe area, Tarim Basin, NW China. *Petrol. Explor. Dev.* **2021**, *48*, 354–366. [[CrossRef](#)]

9. Huang, Y.; He, Z.; He, S.; Tao, Z.; Liu, X.; Luo, T.; Guo, X.; Zhang, D.; Sun, Z.; Dong, T. Fluid geochemical response recorded in the alteration of marine carbonate reservoirs: The Silurian Shiniulan Formation, southeast Sichuan Basin, China. *J. Petrol. Sci. Eng.* **2022**, *208*, 109625. [[CrossRef](#)]
10. Liseroudi, M.H.; Ardakani, O.H.; Pedersen, P.K.; Sanei, H. Fluid flow and water/rock interaction during the Early Triassic evolution of the western Canada sedimentary basin as revealed by carbonate diagenesis. *Mar. Petrol. Geol.* **2022**, *142*, 105765. [[CrossRef](#)]
11. Liu, D.; Zhang, C.; Pan, Z.; Huang, Z.; Luo, Q.; Song, Y.; Jiang, Z. Natural fractures in carbonate-rich tight oil reservoirs from the Permian Lucaogou Formation, southern Junggar Basin, NW China: Insights from fluid inclusion microthermometry and isotopic geochemistry. *Mar. Petrol. Geol.* **2020**, *119*, 104500. [[CrossRef](#)]
12. Qiao, Z.; Shen, A.; Zhang, S.; Hu, A.; Liang, F.; Luo, X.; Shao, G.; Wang, Y.; Zhao, J.; Cao, P. Origin of giant Ordovician cavern reservoirs in the Halahatang oil field in the Tarim Basin, northwestern China. *AAPG Bulletin* **2023**, *7*, 107. [[CrossRef](#)]
13. Wang, R.; Zhang, Y.; Chen, F.; Li, M.; Wen, Z.; Luo, X.; Ding, Z.; Li, B.; Xue, Y. Hydrocarbon fluid evolution and accumulation process in ultradeep reservoirs of the northern Fuman Oilfield, Tarim Basin. *Front. Earth Sci.* **2024**, *12*, 1399595. [[CrossRef](#)]
14. Yu, Z.; Liu, K.; Zhao, M.; Liu, S.; Zhuo, Q.; Lu, X. Petrological record of hydrocarbon accumulation in the Kela-2 gas field, Kuqa Depression, Tarim Basin. *J. Nat. Gas. Sci. Eng.* **2017**, *41*, 63–81. [[CrossRef](#)]
15. Cao, J.; Jin, Z.; Hu, W.; Zhang, Y.; Yao, S.; Wang, X.; Zhang, Y.; Tang, Y. Improved understanding of petroleum migration history in the Hongche fault zone, northwestern Junggar Basin (northwest China): Constrained by vein-calcite fluid inclusions and trace elements. *Mar. Petrol. Geol.* **2010**, *27*, 61–68. [[CrossRef](#)]
16. Jia, L.; Cai, C.; Li, K.; Liu, L.; Chen, Z.; Tan, X. Impact of fluorine-bearing hydrothermal fluid on deep burial carbonate reservoirs: A case study from the Tazhong area of Tarim Basin, northwest China. *Mar. Petrol. Geol.* **2022**, *139*, 105579. [[CrossRef](#)]
17. Nomura, S.F.; Sawakuchi, A.O.; Bello, R.M.S.; Méndez-Duque, J.; Fuzikawa, K.; Giannini, P.C.F.; Dantas, M.S.S. Paleotemperatures and paleofluids recorded in fluid inclusions from calcite veins from the northern flank of the Ponta Grossa dyke swarm: Implications for hydrocarbon generation and migration in the Paraná Basin. *Mar. Petrol. Geol.* **2014**, *52*, 107–124. [[CrossRef](#)]
18. Rddad, L.; Kraemer, D.; Walter, B.F.; Darling, R.; Cousens, B. Unraveling the fluid flow evolution precipitation mechanisms recorded in calcite veins in relation to Pangea rifting–Newark Basin, U.S.A. *Geochemistry* **2022**, *82*, 125918. [[CrossRef](#)]
19. Wei, D.; Gao, Z.; Zhang, L.; Fan, T.; Wang, J.; Zhang, C.; Zhu, D.; Ju, J.; Luo, W. Application of blocky calcite vein LA–MC–ICP–MS U–Pb dating and geochemical analysis to the study of tectonic–fault–fluid evolutionary history of the Tabei Uplift, Tarim Basin. *Sediment. Geol.* **2023**, *453*, 106425. [[CrossRef](#)]
20. Fornero, S.A.; Millett, J.M.; Fernandes De Lima, E.; Menezes De Jesus, C.; Bevilaqua, L.A.; Marins, G.M. Emplacement dynamics of a complex thick mafic intrusion revealed by borehole image log facies analyses: Implications for fluid migration in the Parnaíba Basin petroleum system, Brazil. *Mar. Petrol. Geol.* **2023**, *155*, 106378. [[CrossRef](#)]
21. Jaya, A.; Nishikawa, O.; Sufriadin; Jumadil, S. Fluid migration along faults and gypsum vein formation during basin inversion: An example in the East Walanae fault zone of the Sengkang Basin, South Sulawesi, Indonesia. *Mar. Petrol. Geol.* **2021**, *133*, 105308. [[CrossRef](#)]
22. Zhu, C.; Gang, W.; Zhao, X.; Chen, G.; Pei, L.; Wang, Y.; Yang, S.; Pu, X. Reconstruction of oil charging history in the multisource petroleum system of the Beidagang buried-hill structural belt in the Qikou Sag, Bohai Bay Basin, China: Based on the integrated analysis of oil-source rock correlations, fluid inclusions and geologic data. *J. Petrol. Sci. Eng.* **2022**, *208*, 109197.
23. Ping, H.; Thiéry, R.; Chen, H.; Liu, H. New methods to reconstruct paleo-oil and gas compositions and P–T trapping conditions of hydrocarbon fluid inclusions in sedimentary basins. *Mar. Petrol. Geol.* **2023**, *155*, 106403. [[CrossRef](#)]
24. Song, Y.; Chen, Y.; Wang, M.; Steele-MacInnis, M.; Ni, R.; Zhang, H.; Fan, J.; Ma, X.; Zhou, Z. In situ cracking of oil into gas in reservoirs identified by fluid inclusion analysis: Theoretical model and case study. *Mar. Petrol. Geol.* **2023**, *147*, 105959. [[CrossRef](#)]
25. Duschl, F.; van den Kerckhof, A.; Sosa, G.; Leiss, B.; Wiegand, B.; Vollbrecht, A.; Sauter, M. Fluid inclusion and microfabric studies on Zechstein carbonates (Ca<sub>2</sub>) and related fracture mineralizations–New insights on gas migration in the Lower Saxony Basin (Germany). *Mar. Petrol. Geol.* **2016**, *77*, 300–322. [[CrossRef](#)]
26. Fu, J.; Deng, X.; Wang, Q.; Li, J.; Qiu, J.; Hao, L.; Zhao, Y. Densification and hydrocarbon accumulation of Triassic Yanchang Formation Chang 8 Member, Ordos Basin, NW China: Evidence from geochemistry and fluid inclusions. *Pet. Explor. Dev.* **2017**, *44*, 48–57. [[CrossRef](#)]
27. Shu, Y.; Lin, Y.; Liu, Y.; Yu, Z. Control of magmatism on gas accumulation in Linxing area, Ordos Basin, NW China: Evidence from fluid inclusions. *J. Petrol. Sci. Eng.* **2019**, *180*, 1077–1087. [[CrossRef](#)]
28. Guo, C.; Chen, D.; Qing, H.; Dong, S.; Li, G.; Wang, D.; Qian, Y.; Liu, C. Multiple dolomitization and later hydrothermal alteration on the Upper Cambrian–Lower Ordovician carbonates in the northern Tarim Basin, China. *Mar. Petrol. Geol.* **2016**, *72*, 295–316. [[CrossRef](#)]
29. Huang, Y.; Luo, T.; Tao, Z.; He, Z.; Tarantola, A.; He, S.; Guo, X.; Zhang, D.; Sun, Z. Fluid evolution and petroleum accumulation in the precambrian gas reservoirs of the Sichuan Basin, SW China. *Mar. Petrol. Geol.* **2023**, *150*, 106171. [[CrossRef](#)]
30. Gong, F.; Song, Y.; Zeng, L.; Zou, G. The heterogeneity of petrophysical and elastic properties in carbonate rocks controlled by strike-slip fault: A case study from yangjikan outcrop in the tarim basin. *J. Petrol. Sci. Eng.* **2023**, *220*, 111170. [[CrossRef](#)]
31. Wang, R.; Nie, H.; Hu, Z.; Liu, G.; Xi, B.; Liu, W. Controlling effect of pressure evolution on shale gas reservoirs: A case study of the Wufeng–Longmaxi Formation in the Sichuan Basin. *Natural Gas Industry* **2020**, *40*, 1–11.



32. Wu, G.; Ma, B.; Han, J.; Guan, B.; Chen, X.; Yang, P.; Xie, Z. Origin and growth mechanisms of strike-slip faults in the central Tarim cratonic basin, NW China. *Petrol. Explor. Dev.* **2021**, *48*, 595–607. [[CrossRef](#)]
33. Li, F.; Lü, X.; Zhu, G.; Chen, J.; Wang, R.; Wu, Z.; He, T.; Xue, N. Formation and preservation of ultradeep liquid petroleum in the Ordovician sedimentary succession in Tarim Basin during the neotectonic phase. *J. Asian Earth Sci.* **2023**, *250*, 105645. [[CrossRef](#)]
34. Li, W.; Xu, H.; Yang, J.; Gao, S.; Ning, C.; Yu, Y.; Jiang, T.; Wan, F. Different depositional models of wave-dominated shoreface deposits: An integrated process-oriented analysis (“Donghe sandstones” in Tarim Basin, China). *Mar. Petrol. Geol.* **2023**, *153*, 106288. [[CrossRef](#)]
35. Yao, Y.; Zeng, L.; Mao, Z.; Han, J.; Cao, D.; Lin, B. Differential deformation of a strike-slip fault in the Paleozoic carbonate reservoirs of the Tarim Basin, China. *J. Struct. Geol.* **2023**, *173*, 104908. [[CrossRef](#)]
36. Sun, J.; He, J.; Tao, X.; Guo, S.; Pan, X.; Zhao, K.; Zhang, H.; Yuan, J. Stratigraphic correlation and sedimentology of the Ediacaran succession in the Tarim Basin, NW China: Implications for paleogeographic reconstruction and hydrocarbon exploration. *J. Asian Earth Sci.* **2023**, *247*, 105607. [[CrossRef](#)]
37. Zhao, X.; Wu, C.; Ma, B.; Li, F.; Xue, X.; Lv, C.; Cai, Q. Characteristics and genetic mechanisms of fault-controlled ultradeep carbonate reservoirs: A case study of Ordovician reservoirs in the Tabei paleo-uplift, Tarim Basin, western China. *J. Asian Earth Sci.* **2023**, *254*, 105745. [[CrossRef](#)]
38. Cao, Y.; Wang, S.; Zhang, Y.; Yang, M.; Yan, L.; Zhao, Y.; Zhang, J.; Wang, X.; Zhou, X.; Wang, H. Petroleum geological conditions and exploration potential of Lower Paleozoic carbonate rocks in Gucheng Area, Tarim Basin, China. *Pet. Explor. Dev.* **2019**, *46*, 1165–1181. [[CrossRef](#)]
39. Shen, W.; Chen, J.; Wang, Y.; Zhang, K.; Chen, Z.; Luo, G.; Fu, X. The origin, migration and accumulation of the Ordovician gas in the Tazhong III region, Tarim Basin, NW China. *Mar. Petrol. Geol.* **2019**, *101*, 55–77. [[CrossRef](#)]
40. Zhang, J.; Jiang, Z.; Wang, S.; Wang, R.; Zhang, Y.; Du, W. Bedding-parallel calcite veins as a proxy for shale reservoir quality. *Mar. Petrol. Geol.* **2021**, *127*, 104975. [[CrossRef](#)]
41. Du, Y.; Fan, T.; Machel, H.G.; Gao, Z. Genesis of Upper Cambrian-Lower Ordovician dolomites in the Tahe Oilfield, Tarim Basin, NW China: Several limitations from petrology, geochemistry, and fluid inclusions. *Mar. Petrol. Geol.* **2018**, *91*, 43–70. [[CrossRef](#)]
42. Liu, J.; Li, Z.; Wang, X.; Jiang, L.; Feng, Y.; Wallace, M.W. Tectonic-fluid evolution of an ultradeep carbonate reservoir in the southern Halahatang Oilfield area, Tarim Basin, NW China. *Mar. Petrol. Geol.* **2022**, *145*, 105870. [[CrossRef](#)]
43. Wang, X.; Wang, J.; Cao, Y.; Han, J.; Wu, K.; Liu, Y.; Liu, K.; Xie, M. Characteristics, formation mechanism and evolution model of Ordovician carbonate fault-controlled reservoirs in the Shunnan area of the Shuntuogole lower uplift, Tarim Basin, China. *Mar. Petrol. Geol.* **2022**, *145*, 105878. [[CrossRef](#)]
44. Ping, H.; Chen, H.; George, S.C.; Li, C.; Hu, S. Relationship between the fluorescence color of oil inclusions and thermal maturity in the Dongying Depression, Bohai Bay Basin, China: Part 2. fluorescence evolution of oil in the context of petroleum generation, expulsion and cracking under geological conditions. *Mar. Petrol. Geol.* **2019**, *103*, 306–319.
45. Zhou, X.; Lü, X.; Zhu, G.; Cao, Y.; Yan, L.; Zhang, Z. Origin and formation of deep and superdeep strata gas from Gucheng-Shunnan block of the Tarim Basin, NW China. *J. Petrol. Sci. Eng.* **2019**, *177*, 361–373. [[CrossRef](#)]
46. Ni, Z.; Wang, T.; Li, M.; Fang, R.; Li, Q.; Tao, X.; Cao, W. An examination of the fluid inclusions of the well RP3-1 at the Halahatang Sag in Tarim Basin, northwest China: Implications for hydrocarbon charging time and fluid evolution. *J. Petrol. Sci. Eng.* **2016**, *146*, 326–339. [[CrossRef](#)]
47. Xu, Z.; Liu, L.; Wang, T.; Wu, K.; Gao, X.; Dou, W.; Xiao, F.; Zhang, N.; Song, X.; Ji, H. Application of fluid inclusions to the charging process of the lacustrine tight oil reservoir in the Triassic Yanchang Formation in the Ordos Basin, China. *J. Petrol. Sci. Eng.* **2017**, *149*, 40–55. [[CrossRef](#)]
48. Gao, J.; He, S.; Zhao, J.; Yi, J. Geothermometry and geobarometry of overpressured lower Paleozoic gas shales in the Jiaoshiba field, Central China: Insight from fluid inclusions in fracture cements. *Mar. Petrol. Geol.* **2017**, *83*, 124–139. [[CrossRef](#)]
49. Su, A.; Chen, H.; Lei, M.; Li, Q.; Wang, C. Paleo-pressure evolution and its origin in the Pinghu slope belt of the Xihu Depression, East China Sea Basin. *Mar. Petrol. Geol.* **2019**, *107*, 198–213.

**Disclaimer/Publisher’s Note:** The statements, opinions and data contained in all publications are solely those of the individual author(s) and contributor(s) and not of MDPI and/or the editor(s). MDPI and/or the editor(s) disclaim responsibility for any injury to people or property resulting from any ideas, methods, instructions or products referred to in the content.